# Calibrated ratio approach for vegetation detection in shaded areas

Hung-Ming Kao
Hsuan Ren
Chao-Shing Lee

**SPIE.**

# Calibrated ratio approach for vegetation detection in shaded areas

**Hung-Ming Kao,**[a,*] **Hsuan Ren,**[a] **and Chao-Shing Lee**[b]

[a]National Central University, Center for Space and Remote Sensing Research, No. 300, Jhong-Da Road, Jhongli City, Taoyuan County 32001, Taiwan

[b]National Taiwan Ocean University, Institute of Applied Geosciences, No. 2. Pei-Ning Road, Keelung 20224, Taiwan

**Abstract.** Removing shadow effects remains a challenge in processing optical remote sensing data. Shadows occur because of obstructions from the terrain topography or cloud cover, which can cause errors for image classification. Shadow effects can be removed using a band-ratio approach because the shaded areas in optical images have a nearly proportional variation in the bands. We developed a calibrated band-ratio approach for shadow reduction. Before the ratio approach was applied, a regression technique was used to obtain information for calibration from the relative sensor gain and offset. After calibration, the ratio vegetation index (RVI) band ratios were calculated to process the image data, which can simultaneously remove the shadow effects and assist the search for vegetation. Real and synthesized images show that the calibrated-ratio approach can improve vegetation detection compared with standard RVI and dark pixel subtraction approaches. © *The Authors. Published by SPIE under a Creative Commons Attribution 3.0 Unported License. Distribution or reproduction of this work in whole or in part requires full attribution of the original publication, including its DOI.* [DOI: 10.1117/1.JRS.8.083543]

## 1 Introduction

The solar zenith angle is usually not nadir when satellites or airborne sensors are collecting data. The topographic effects, therefore, introduce shadows in remotely sensed images, especially in mountainous areas. Similarly, most inhabited mountainous regions are usually covered by vegetation, which can be detected using vegetation indexes. Most of the indexes, ratio vegetation index (RVI), spectral vegetation index (SVI), and normalized difference vegetation index (NDVI), utilize the ratios of specific channels in multispectral or hyperspectral images.[1] In this study, a novel algorithm is developed to reduce topographic effects using the ratio approach, similar to the approach used in the usual indexes. The proposed algorithm employs the characteristics of mountainous regions that are usually covered by vegetation and can detect vegetation and reduce shadow effects simultaneously.

Shadows characteristically have lower reflectance intensity than unshaded areas, and shadow effects also influence the spectral character. Therefore, shadow effects cause errors in the identification and classification of terrain and vegetative cover so that shadow removal is necessary before processing. Shadow effects in optical remote sensing have been discussed by several groups.[2–6] Because topographic effects are highly correlated with the terrain and geometry between the solar zenith and sensor, using both measurements and simulation, the relationship between topographic effects and spectral responses can be understood quantitatively. Digital elevation models (DEM) are used to provide information on terrain for geometric and radiometric corrections.

---

*Address all correspondence to: Hung-Ming Kao, E-mail: hartge1020@yahoo.com.tw

According to radiation transform theory, signals have three components for detection by sensors, including an unscattered surface-reflected component, a downscattered surface-reflected skylight, and an upscattered path radiance.[1] The first component (unscattered surface-reflected) includes information on the geometry between solar elevation and the topographic surface as a cosine term,[7] and this information can be obtained from a DEM in rugged terrain. Using a DEM simulation is a direct way to estimate shaded-relief images,[7–9] which is able to predict shadows in a mountainous terrain. There have been numerous successful approaches to correct (lighten) shadow effects in multispectral images using DEM analysis.[10–17] The main principle uses the relationship between solar elevation and topographic surface to calibrate shaded spectra to a normal level. This approach requires information on terrain to help simulate or correct the spectral bands. Similar methods can also be applied to hyperspectral images[18] and use a Sun-canopy-sensor for forest images.[19–21] The DEM shadow simulation could also help radar measurements for aviation safety.[22] However, because of heavy computational requirements and the lack of fine resolution of DEMs in mountainous regions, the DEM approach may cause difficulties for topographic correction.

Another approach uses shadow detection. These methods only use information from the images to eliminate shadows. The concept of this approach is similar to that for detecting a shadow in the image and calibrating the shaded pixels to normal intensity.[23–31] The challenge of these approaches is that some spectra are similar to shadows (e.g., water or dark pixels) and are difficult to discriminate. Most of the approaches use advanced mathematical methods to identify shaded pixels and calibrate them precisely. With improvement in statistical techniques, these approaches could provide less ambiguous results. By applying the shadow-detection technique to cloudy and temporal images, a clear-sky composite image (less shadow and fewer clouds) can be obtained.[32] In addition to satellite and airborne remote sensing, visual intelligence also employs similar principles to reduce or eliminate shadow effects, which does not need any topographic or spatial information.[33,34] Even though the topographic information is not necessary in these approaches, the complexity and computational needs are concerns.

The multispectral image for a shaded area causes a phenomenon where some channels decrease proportionally. This phenomenon can be used to reduce shading effects by calculating ratios among the bands.[1,35–37] The band-ratio approach is the simplest method to reduce topographic effects; however, additional factors (from the atmosphere and instruments in Ref. 1) are usually involved in the spectral signals. Before using the band-ratio approach, the spectral data should be processed to remove these additional factors.[38,39] There have been several approaches applying multispectral ratios to reduce topographic effects.[36,40–43] In addition to multispectral ratios, the hyperspectral ratio approach also has been discussed,[44] and studies of both systems (multispectral and hyperspectral) are employed to determine spectral gain and offset before processing. In this study, several simple relative parameters (combined path radiance and sensor offset term) are developed to substitute for the absolute parameters (gain and offset, from atmosphere and instruments). The proposed algorithm utilizes a new concept using relative parameters for band ratios to reduce topographic shadow effects. In addition, the algorithm uses only the original digital number (DN) image and does not need any complex radiometric calibration, such as radiance or reflectance.

In tropical and subtropical zones, vegetation coverage is very important to understand the potential for landslide and debris flow, especially in mountainous regions. However, topographic shadows can cause serious errors in interpreting remote images from mountainous areas. We propose a novel algorithm to eliminate shadow effects using a well-known property (band ratio) of multispectral images. The algorithm does not use any topographic information or shadow-detection approaches. Instead, we use a simple way to reduce shadows and detect vegetation coverage at the same time. The results presented here show that the algorithm deals with the shadow-removal problem effectively in a mountainous terrain.

## 2 Methods

Most mountainous areas (from tropical to temperate zones) are usually covered by vegetation, and remotely sensed images suffer from shadow effects. The vegetation indexes (i.e., RVI, SVI,
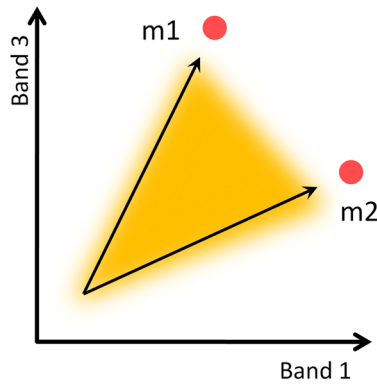
**Fig. 1** Bispectral scatter plot for a rugged surface. The spectra distributed along the axes represent the shadow; m1 and m2 represent two different spectra, respectively.

and NDVI) not only amplify vegetation signals, but also reduce shadow effects using a band ratio. Here, the proposed algorithm uses the band-ratio approach to enhance signals for vegetated areas and reduce shadow effects.

Theoretically, in a bispectral scatter plot, the pixels of one material should concentrate on a point, and this property can be used to classify the spectra using a distance calculation (i.e., Euclidean and City Block distance). However, in rough terrain, the spectra will form a straight line (Fig. 1) and spectra along the line have the same slope (band ratio).[1,36] Therefore, the ratio plots should contain information on the topographic shadows that enable the reduction of the shadow effects.

Reference 36 showed that using the band ratio can reduce terrain effects by removing the cosine factor (the angle between solar and topography), provided the gain and offset (the contribution from path radiation and satellite sensors) are estimated before calculating the ratio.[39,40] Figure 2 explains the influence of classification (or detection) performance using a ratio approach before and after additional factors (gain and offset) are subtracted.[39] Figures 2(a)
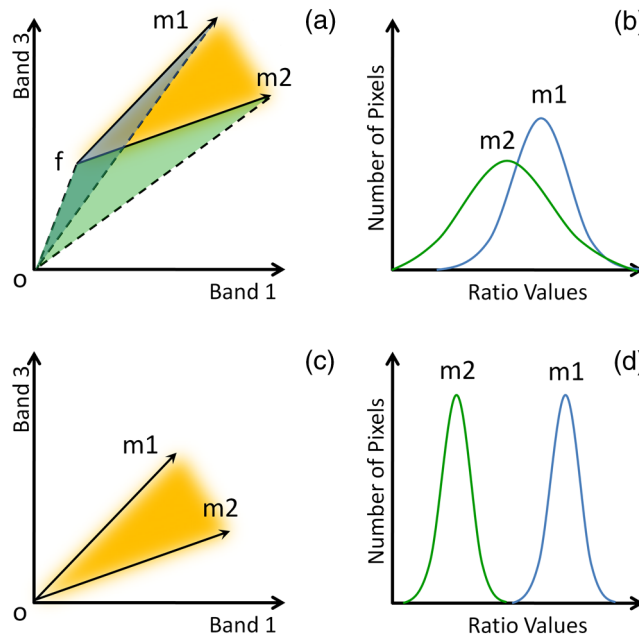


**Fig. 2** Bispectral scatter plot and histogram corresponding to the ratio image.[39] (a) The yellow region (△ f m1 m2) shows a scatter plot (unadjusted), the blue region (△ o f m1) represents the ratio of spectra 1, and the green region (△ o f m2) represents the ratio of spectra 2. (b) Histogram for ratios corresponding to m1 and m2. (c) Scatter plot shows the image after adjustment. (d) Histogram for ratios corresponding to m1 and m2.
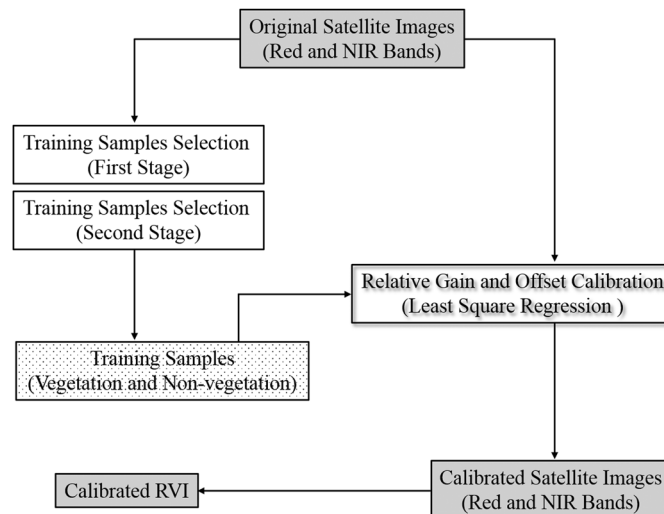
```
┌─────────────────────────────┐
│  Original Satellite Images  │
│     (Red and NIR Bands)     │
└─────────────────────────────┘
```

**Fig. 3** Flow chart of the proposed method [calibrated ratio vegetation index (RVI)].

and 2(b) show the ratios before subtraction. Some pixels might not be separated with the ratio approach. After additional factors are subtracted, the ratio approach is capable of correctly separating the two spectra [Figs. 2(c) and 2(d)].

In traditional approaches, the parameters (gain and offset) are obtained by direct measurements or by searching the images.[36] These methods can obtain absolute gain and offset required for unbiased analysis of images. However, the values of atmosphere-pass radiation and sensor contribution may not be obtainable. We, therefore, utilize a novel concept to estimate the relative gain and offset when calculating the ratio of the spectral bands. Figure 3 shows the flow chart of the proposed algorithm. By assigning the vegetated and nonvegetated pixels as training samples, the relative parameters (relative gain and offset) can be estimated. Then these relative parameters can be used with the images to compute the band ratio or other vegetation indexes, enabling the shadow effects to be reduced while the vegetated area is enhanced.

## 2.1 Band-Ratio Approach

In multispectral images, observations for a shaded region usually decrease proportionally in all bands. This property can be used to reduce shadow effects using a ratio. Equation (1) shows a simple two-dimensional radiation-transform function that includes several elements affecting the observation value by satellite sensors:

$$DN(x, y) = a\rho(x, y)\cos[\theta(x, y)] + b. \qquad (1)$$

$DN(x, y)$ is the DN observed from the satellite sensor, $a$ and $b$ are the gain and offset of the sensor representing the atmosphere and instrument contribution, $\rho(x, y)$ is the radiance $(W/m^2/sr/\mu m)$, which corresponds to the energy of the response from the ground, and $\theta(x, y)$ is the angle between the topographic surface and the sun.

From Eq. (1), $\cos[\theta(x, y)]$ can be regarded as the effective portion of the value from the topography and solar position. The band ratio is a well-known approach[1] to divide two bands to remove this angular element.

$$RATIO = \frac{[DN_m(x, y) - b_m]/a_m}{[DN_n(x, y) - b_n]/a_n} = \frac{\rho_m(x, y)\cos[\theta(x, y)]}{\rho_n(x, y)\cos[\theta(x, y)]}. \qquad (2)$$

In Eq. (2), the sensor observation has been calibrated with additional factors (gain and offset). After dividing either of the two bands ($m$ and $n$), the $\cos[\theta(x, y)]$ terms cancel and the shadow effects should be eliminated. The RVI method[1] uses the principle of Eq. (2).

$$\text{RVI} = \frac{\rho_{\text{NIR}}(x, y)}{\rho_{\text{red}}(x, y)}. \tag{3}$$

The RVI method utilizes the property of vegetation spectra where the near-infrared-light (NIR) band is usually higher than the red-light band, and detecting or enhancing the vegetation signal can be accomplished using Eq. (3). Equation (3) also shows the $\cos[\theta(x, y)]$ terms cancelled by division; therefore, the RVI not only detects vegetation, but also lightens or removes the shadow effects.

## 2.2 *Gain and Offset Acquisition*

From Eq. (2), an unbiased ratio should include a calibrated gain and offset [Eq. (2), $a$ and $b$] before any signal processing.[39,40] The traditional approach measures these factors in the field or using instruments. In addition to actual measurements, some approaches utilize statistical methods to estimate the parameters using only remote-sensing images.[36] In this study, a relative gain and offset concept is defined by selecting training samples in certain areas. The relative parameters can then be estimated and used as an unbiased ratio without incorporating atmospheric or other instrumental measurements.

First, we suppose that there are two training-sample regions and each contains only a single material (vegetated and nonvegetated), and both of the regions are affected by topographic shadows. After calibration using the gain and offset, the slopes (ratio value) should be constant [Fig. 1, Eqs. (4) and (5)]. According to the definition of NDVI, [1] the value will be between $-1$ and 1. However, practical experience[45] indicates that the NDVI value should be ~0.6 for vegetation and 0.2 for a soil surface (nonvegetated). These two established thresholds were selected as target parameters for band ratios. The NDVI can then be transformed to RVI. In Eq. (4), the training sample is vegetated and the ratio should be ~4. For Eq. (5), the ratio for the nonvegetated training sample should be ~1.5:

$$\frac{[\text{DN}_m(x, y) - b_m]/a_m}{[\text{DN}_n(x, y) - b_n]/a_n} = 4, \tag{4}$$

$$\frac{[\text{DN}_m(x, y) - b_m]/a_m}{[\text{DN}_n(x, y) - b_n]/a_n} = 1.5. \tag{5}$$

After simplifying Eqs. (4) and (5), Eqs. (6) and (7) can be derived:

$$\text{DN}_m(x, y) = 4 \cdot \frac{a_m}{a_n} \cdot \text{ND}_n(x, y) + b_m - 4 \cdot \frac{b_n \cdot a_m}{a_n}, \tag{6}$$

$$\text{DN}_m(x, y) = 1.5 \cdot \frac{a_m}{a_n} \cdot \text{ND}_n(x, y) + b_m - 1.5 \cdot \frac{b_n \cdot a_m}{a_n}. \tag{7}$$

If we assign $X = \frac{a_m}{a_n}$, $Y = b_m$, and $Z = b_n \cdot \frac{a_m}{a_n}$, Eqs. (6) and (7) are arranged to Eqs. (8) and (9):

$$\text{DN}_m(x, y) = 4 \cdot X \cdot \text{DN}_n(x, y) + Y - 4 \cdot Z, \tag{8}$$

$$\text{DN}_m(x, y) = 1.5 \cdot X \cdot \text{DN}_n(x, y) + Y - 1.5 \cdot Z. \tag{9}$$

In Eqs. (8) and (9), $X$, $Y$, and $Z$ are unknown terms, and the known terms include $\text{ND}_m(x, y)$ and $\text{ND}_n(x, y)$ (training samples). The training samples in Eqs. (8) and (9) are obtained from a vegetated and a nonvegetated region, respectively. Both classifications (vegetated and nonvegetated) are selected as training samples to constrain the values of RVI (vegetated: 4, nonvegetated:

1.5). The training-sample spectra are processed by a least-squares (LS) approach with Eqs. (8) and (9), and the system parameters $X$, $Y$, and $Z$ are obtained. These parameters only represent the relationship between the band pairs [Eqs. (6) and (7)], so we declare $X$, $Y$, and $Z$ as the relative additional factors (relative gain and offset).

After the acquisition of relative gain and offset, $X$, $Y$, and $Z$ can be substituted into Eqs. (6) and (7) to obtain the relative calibration. The calibrated results are used to calculate the band ratios by Eqs. (10) and (11). Figure 3 shows the flow chart of the calibrated processing.

$$\text{RATIO} = \frac{\text{DN}_m(x, y) - Y}{\text{DN}_n(x, y) \cdot X - Z} = 4, \tag{10}$$

$$\text{RATIO} = \frac{\text{DN}_m(x, y) - Y}{\text{DN}_n(x, y) \cdot X - Z} = 1.5. \tag{11}$$

## 2.3 Training-Sample Selection

Figure 1 shows a red-NIR scatter plot for a mountainous region. Using this scatter plot, all pixels can be decomposed by two endmembers, which include vegetated and nonvegetated regions (m1 and m2). In rugged terrain, each class (endmember, pixel group) will be distributed along a straight line,[39,40] and this property can be utilized to select the training samples automatically. Figure 4 shows a graph describing the training-sample selection in the red-NIR scatter plot. The training samples are selected to contain one classification and include a range of signals for shaded areas (from non, light, medium, and heavy shadows) as well. The pixels for a vegetated area should be distributed along the axis that has the highest slope (ratio). The automatic selection approach is used to search the minimal pixels in each slice of the NIR band
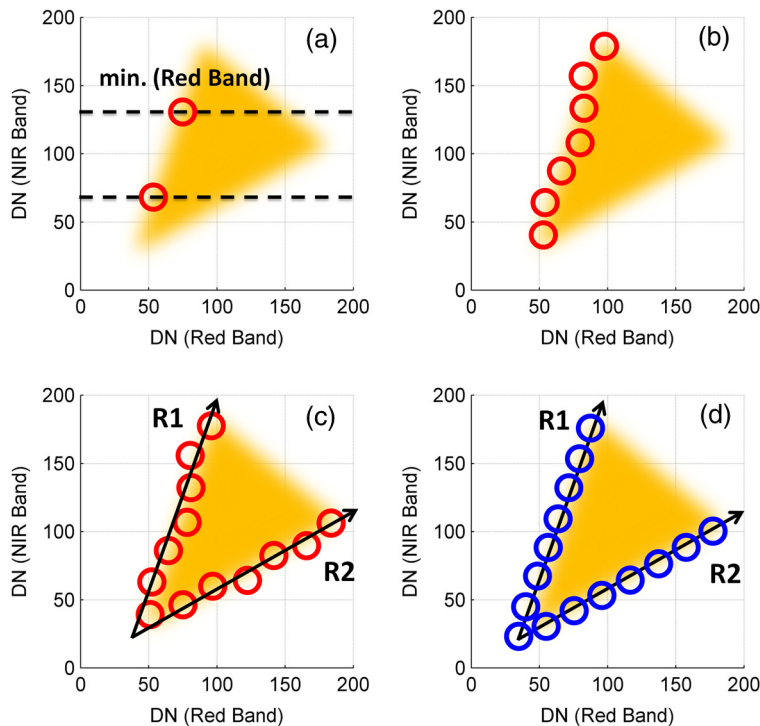


**Fig. 4** Plots showing the selection of training samples. (a) Minimum points searching (red band) in each near-IR (NIR) digital number (DN). (b) The points with minimum red bands can be selected (red circles). (c) Vectors R1 and R2 are obtained by regression from the training samples selected in (b) (red circles). (d) The final training samples (blue circles) selected by vectors R1 and R2.

[Figs. 4(a) and 4(b)]. In addition, pixels for nonvegetated areas with a lower slope (ratio) are also distributed along the other axis and can be obtained by searching for the minimal pixels in each slice of the red band [similar to Figs. 4(a), 4(b), and 4(c)].

However, outlier pixels may interfere with the distribution in the red-NIR scatter plot so that the training samples do not lie along a straight line [Figs. 4(b) and 4(c)]. Outliers are suppressed by a two-stage process. After the first stage of training-sample selection, the rough training samples are selected [Figs. 4(a) and 4(b)]. The second stage uses simple regression for the selected training samples to obtain the vectors [Fig. 4(c), R1 and R2]. Each vector represents the end-members of vegetated and nonvegetated spectra. The algorithm uses the vectors as the axes to search the pixels that are close to the axes at the second-stage training-sample selection [Fig. 4(d)]. To obtain sufficient training samples, the number of pixels must exceed a critical value. The recommended number of training samples should exceed 1% of the total pixels, and the proportion of vegetated and nonvegetated data should be equal. By applying this automatic two-stage process, the training-sample selection approach is both objective and performs well in eliminating interference from outliers.

After selecting the training samples, the selected pixels can be used to solve Eqs. (8) and (9) by LS regression to obtain the relative parameters ($X$, $Y$, and $Z$). Application of the relative parameters to the calibrated RVI [Eqs. (10) and (11)] provides a shadow-free image.

## 3 Results

Two methods for reducing the effects of shadows were compared using actual and simulated image sets: the standard, DPS (dark pixel subtraction), and calibrated RVIs (standard, DPS, and calibrated NIR/red ratio). We selected a set of satellite and synthetic images for a mountainous region, which included shadow effects for this evaluation.

### 3.1 Actual Image

Because most of the high-resolution resource satellites are polar orbiting (Sun synchronous orbiting), the viewing angle between the sensor and ground is usually not nadir so that the sunlight is not directly overhead. Therefore, images collected in rugged terrain usually have serious shadow effects, which can lead to errors.

### 3.1.1 SPOT satellite images

A SPOT5 multispectral image set (Figs. 5 and 6) from a mountainous area in Jianshi (northern Taiwan) was used for the comparison. These images have only been geometrically corrected and the DN is 8-bit scale. In the images, there are several classifications, such as vegetation, riverbed, exposed soil, and buildings. Figure 5 shows that, in general, the spectra can be classified into vegetated and nonvegetated regions. The goal of the proposed algorithm is to exclude shadow effects and simultaneously detect the vegetated cover.

Figure 6 shows a SPOT5 image set from band 1 to band 4 (band 1: green light 500 to 590 nm, band 2: red light 610 to 680 nm, band 3: NIR 780 to 890 nm, band 4: short-wave IR 1,580 to 1750 nm). Shaded areas have low values for all bands, making the data ideal for testing the effectiveness of ratios of band pairs for reducing shadow effects. However, before calculating the ratio, the image should be calibrated using a gain and offset term to prevent biases.

According to Fig. 1, areas with the same classification will be distributed along an axis on a bispectral scatter plot. If there are shadow effects, all of the pixels classified as vegetated (Fig. 1) should have a uniform slope (ratio) in the red-NIR scatter plot, and each class should also be distributed along an axis with a particular slope (ratio). In an actual satellite image, this feature can be observed in the SPOT5 red-NIR scatter plot (Fig. 7). In Figs. 5, 6, and 7, a vegetated area was selected [green rectangle; Fig. 7(a)], and in the bispectral scatter plot, (red-NIR), the vegetated pixels would be distributed along an axis [Fig. 7(b)]. Because of the shadow effect, pixels in each class would be distributed along a straight line, to constitute with several classes the scatter distribution appeared to be a triangle [Fig. 7(b)] as anticipating with Sec. 2 in Fig. 1.
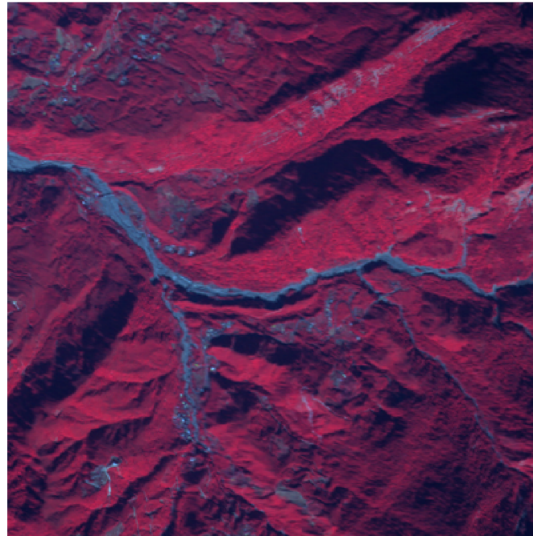
Color map



**Fig. 5** This SPOT5 satellite image was acquired on December 23, 2005, at 10:21 a.m. (Jianshi, northern Taiwan). The area is 4 km × 4 km and the spatial resolution is 10 m/pixel. The color was stacked by R-G-B in bands 3, 2, and 1 (NIR, red light and green light) and the topographic shadows can be easily seen.
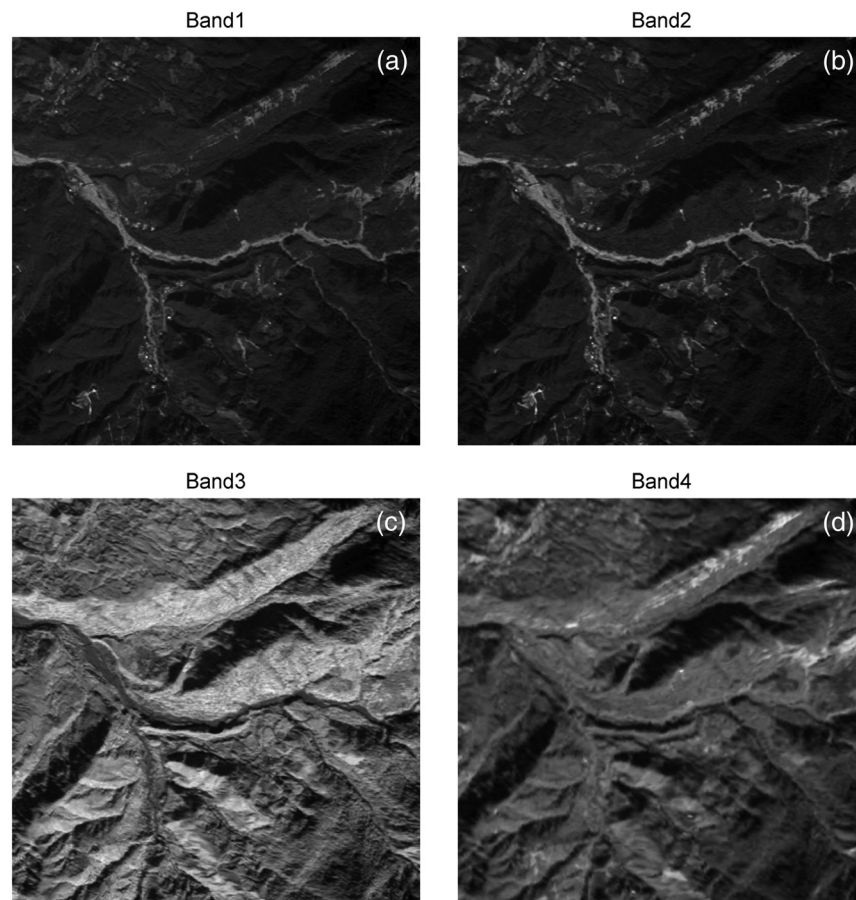
Band1

Band2



Band3

Band4



**Fig. 6** The SPOT5 satellite image set. (a) Band 1 (green). (b) Band 2 (red). (c) Band 3 (NIR). (d) Band 4 (short-wave IR).
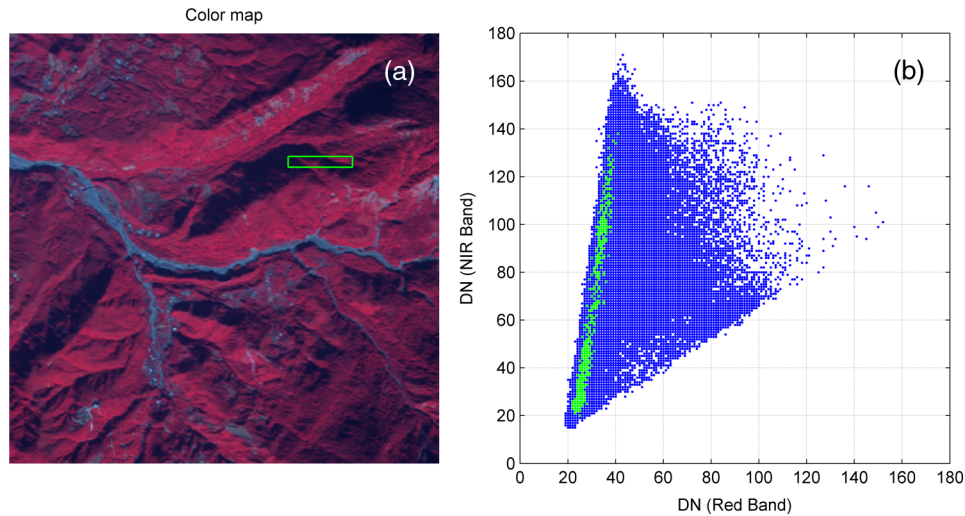
**Fig. 7** Bispectral distribution of SPOT5 satellite image. (a) Color map. The green rectangle shows the area including the training samples. (b) Scatter plot of band 2 (red) and band 3 (NIR). The green pixels are the selected training samples.

### 3.1.2 *Shadow removal*

In Sec. 2.3, an automatic training-sample selection method was discussed in which the minimal pixels in each slice of the NIR and red bands are searched (Fig. 4). Pixels for vegetated and nonvegetated areas were selected as the training samples (Fig. 8). The manually selected results [Fig. 7(b)] and the results using the automatic method [Fig. 8(a)] show a similar distribution of pixels. In Fig. 8(a), the training samples were selected in the first stage (Sec. 2.3). For extreme values (very high or very low DN values), the training selection was affected by outlier pixels [Fig. 8(a)]. This problem was solved in the second stage of the selection process (Sec. 2.3). Figure 8(b) shows that the outliers were removed and the selected pixels are distributed reasonably. In this case, only 1% of pixels have been selected as the training samples (~1600 pixels), and the proportion of vegetated and nonvegetated is the same.

The initial gray-scale values (DN) in Figs. 9(a) and 9(b) display the training samples in ascending order. The NIR has a higher contrast than the red band. The RVI (NIR/red ratios) values are shown in Figs. 9(c) and 9(d). Although the ratio approach was used, the shadow effect on RVI is still evident [Fig. 9(c)]. After linear regression for band 2 (red) and band 3 (NIR) using Eqs. (7) and (8), the relative gain and offset (X, Y, and Z) are obtained. We then use X, Y, and Z to calibrate the images and compute the RVI using Eqs. (10) and (11) to obtain the results in Figs. 10(a) and 10(b). The nonvegetated ratio is slightly overestimated for an extreme dark area
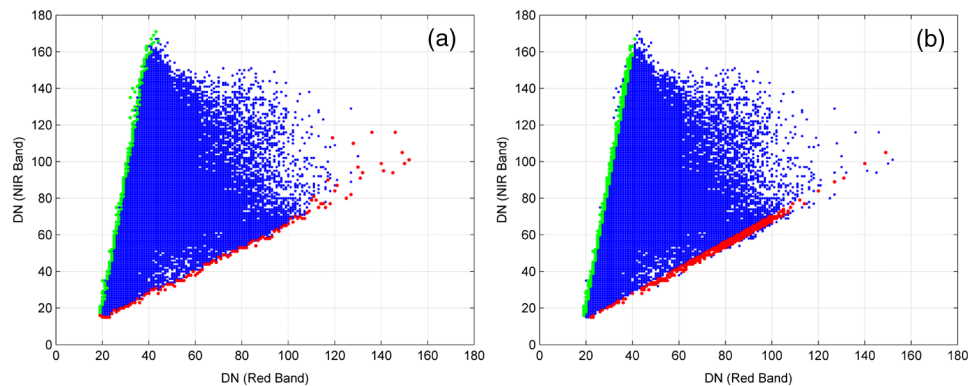


**Fig. 8** Scatter plot for the training sample selection in red-NIR bands (blue points are pixels, green points indicate the selected vegetated training data, and red points indicate the selected nonvegetated training data.) (a) Training sample selection at the first stage. (b) Training sample selection at the second stage.
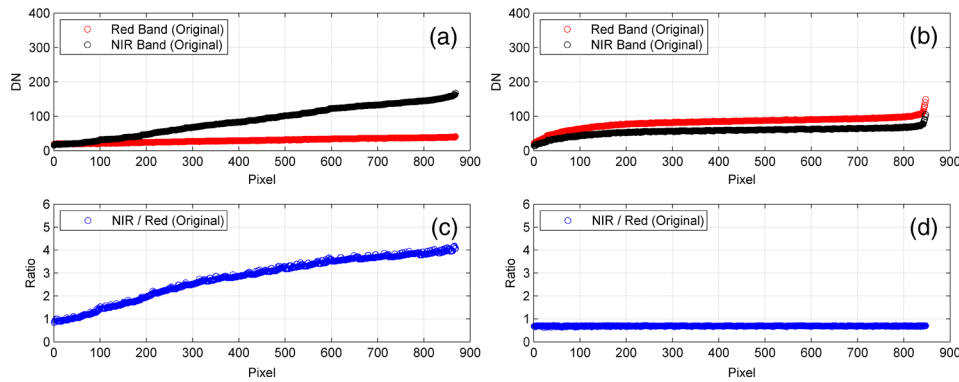
**Fig. 9** Gray-scale values (DN, red and NIR bands) and ratios of the initial training samples. (a) Vegetated training samples. (b) Nonvegetated training samples. (c) RVI of vegetated training samples. (d) RVI of nonvegetated training samples.
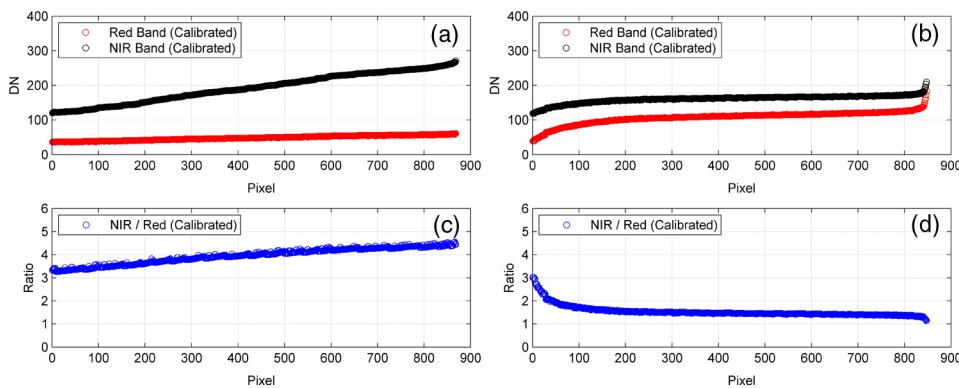


**Fig. 10** Gray-scale values (DN, red, and NIR bands) and ratios of the calibrated training samples. (a) Vegetated training samples. (b) Nonvegetated training samples. (c) RVI for the vegetated training samples. (d) RVI for the nonvegetated training samples.

[Fig. 10(d)]. In general, the RVI shows a uniform value for shadow and nonshadow areas in Figs. 10(c) and 10(d), indicating that the shadow has only small effects on these two indexes after calibration.

### 3.1.3 Comparisons

Our method uses training samples to calibrate bands before the RVI is calculated to obtain an unbiased ratio to reduce shadow effects. Comparing the RVI between the initial and calibrated training samples (Figs. 9 and 10), the calibrated results show that shadow effects were greatly reduced and both vegetated and nonvegetated areas can be clearly distinguished. Applying the calibrated RVI to the entire image, the performance of the comparison of vegetation indexes is shown in Fig. 11.

Comparisons of standard, DPS, and calibrated RVI are shown in Fig. 11. Figures 11(a), 11(b), and 11(c) show serious shadow effects. Figure 11(b) shows that the standard RVI without any processing before band ratioing has obvious shadow effects. Figure 11(c) is the DPS RVI, which subtracts the minimum DN pixel value before ratioing. Using the standard RVI, erroneous estimates for vegetated cover can be gained [shown in Fig. 11(b)]. By DPS RVI, the shadow effects have slightly reduced. Figure 11(d) shows the RVI result using the calibration method. The shadow effect is significantly reduced, and the vegetated cover can be estimated more accurately.

### 3.1.4 Performance evaluation

A set of real satellite images has enabled a quantitative evaluation of the proposed method. Figure 12 shows the shaded image sets, which are distributed in mountainous areas in
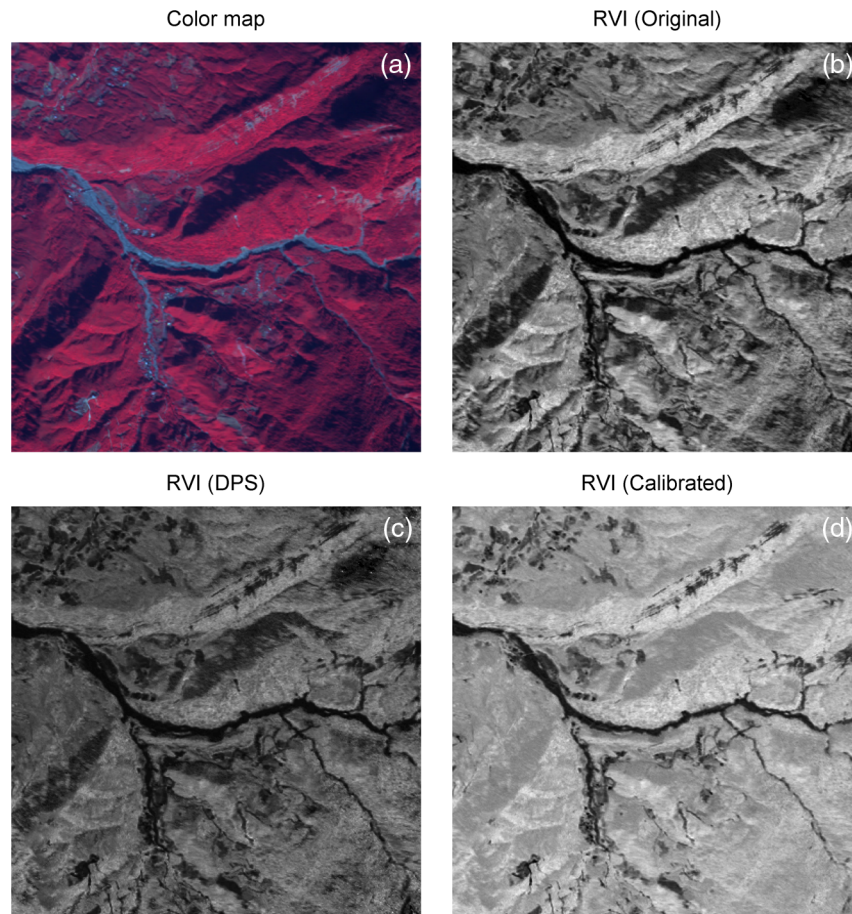
Color map

RVI (Original)



RVI (DPS)

RVI (Calibrated)

**Fig. 11** Comparisons of different adjustment approaches in real satellite images. (a) Color map. (b) Standard RVI. (c) Dark pixel subtraction (DPS) RVI. (d) Calibrated RVI (proposed algorithm).

Taiwan. Table 1 also shows information on the image sets: multispectral images from two different satellite sensors (SPOT5 and Formosat2) in four different areas (Jianshi, Guguan, Jiufen, and Caoling). After processing by RVIs (standard, DPS, and calibrated), the maximum likelihood (ML) classification algorithm converts the RVIs into binary results so that each pixel is classified into vegetated or nonvegetated coverage. There are 100 random check points selected from each area for error analysis, and the ground truth data are judged subjectively using high-resolution color maps (panchromatic fusion, Formosat2: 2 m/pixel, SPOT5: 2.5 m/pixel). Table 1 shows that the vegetation detection accuracy of calibrated RVIs is significantly better than other RVIs not only in all four test scenes, but also in two multispectral satellite sensors.

## 3.2 Simulated Image

A simulated image set was used to assess the performance of the new method. The abundances of two classes (vegetated and nonvegetated) were defined and spectra acquired from a real SPOT5 satellite image. After combining the abundances and the spectra to form a nonshadow simulated image set, a two-dimensional shadow function was applied to the synthetic image set. Noise was also added to the synthetic image sets to simulate more realistic conditions.

### 3.2.1 Simulated images

The sine function was used to produce the two-dimensional classification abundances. Since the abundances are allowed to sum to one and non-negative constrains, the range varies from 0 to 1. The abundances of the two classifications representing vegetated and nonvegetated areas in the frame are shown in Fig. 13.
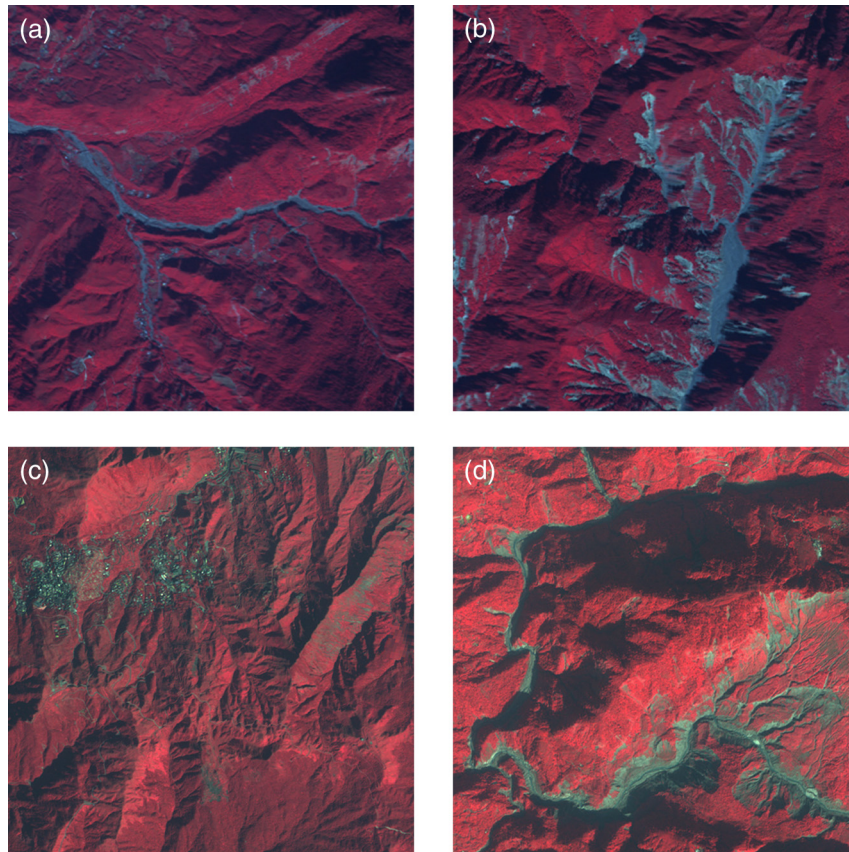
**Fig. 12** Real satellite image sets in mountainous areas. (a) SPOT5 image in Jianshi (north Taiwan). (b) SPOT5 image in Guguan (central Taiwan). (c) Formosat2 image in Jiufen (north Taiwan). (d) Formosat2 image in Caoling (south Taiwan). The color was stacked by R-G-B in NIR, red light, and green light bands.

**Table 1** Comparison of the performance of standard ratio vegetation index (RVI), dark pixel subtraction (DPS) RVI, and calibrated RVI.

| Region of Taiwan | Taiwan (north) | Taiwan (central) | Taiwan (north) | Taiwan (south) |
|---|---|---|---|---|
| Place name | Jianshi | Guguan | Jiufen | Caoling |
| Satellite sensor | SPOT5 | SPOT5 | Formosat2 | Formosat2 |
| Date acquired | December 23, 2005 | December 23, 2005 | February 13, 2009 | January 2, 2011 |
| Area | 4 km × 4 km | 4 km × 4 km | 4 km × 4 km | 4 km × 4 km |
| Spatial resolution | 10 m/pixel | 10 m/pixel | 8 m/pixel | 8 m/pixel |
| Spectral channels | Red and near-IR | Red and near-IR | Red and near-IR | Red and near-IR |
| Vegetation detection accuracy (std. RVI) | 83% | 93% | 89% | 94% |
| Vegetation detection accuracy (DPS RVI) | 92% | 93% | 90% | 93% |
| Vegetation detection accuracy (calib. RVI) | 95% | 98% | 96% | 98% |
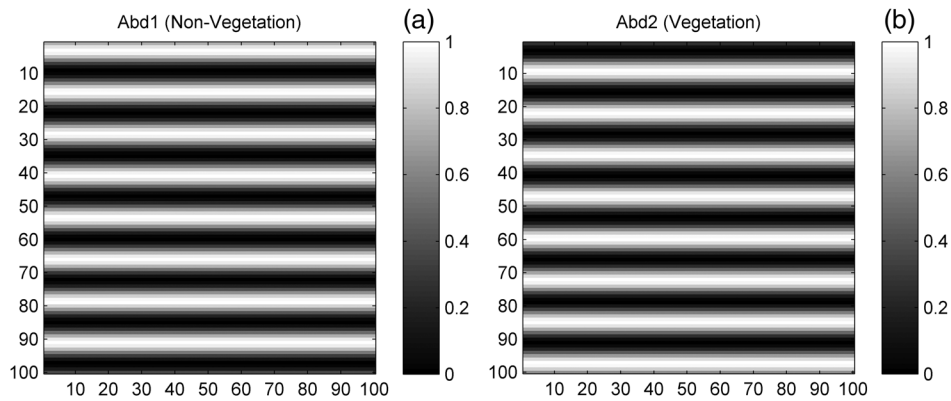
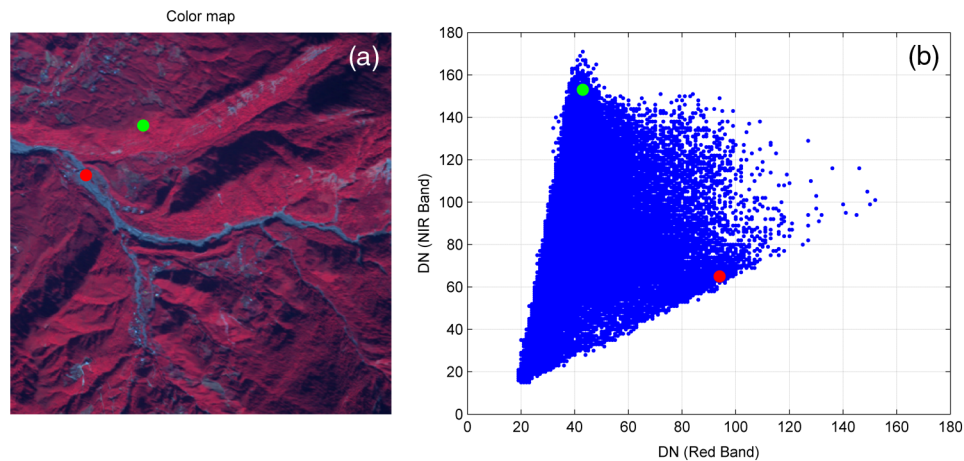**Fig. 13** Simulated abundances of two classes: (a) nonvegetated abundance and (b) vegetated abundance.



**Fig. 14** Spectra from the SPOT5 image. (a) The two spectra pixels are shown on the color map. The red point is nonvegetated and the green point is vegetated. (b) The spectra pixels on a red-NIR scatter plot where the blue points are all of the pixels, the red point is nonvegetated, and the green point is vegetated.

After the initial abundance model was built, the simulated image used actual satellite image spectra to form the synthetic image set. The spectra acquired from the SPOT5 image (Fig. 14) included vegetated and nonvegetated areas. In Fig. 14(a), the vegetated and nonvegetated areas were selected from a nonshadow region. The green point is on a vegetated pixel and the red point is on a river bed. In Fig. 14(b), the red-NIR scatter plot shows the distribution of the vegetated and nonvegetated endmembers. These abundances were multiplied with the spectra of vegetated and nonvegetated areas acquired from actual satellite images (Fig. 14) to obtain the initial simulated image.

To simulate the topographic effect, a shading function was designed with a range from 0 to 1 (Fig. 15). Figure 15(a) shows the two-dimensional shadow function, and Fig. 15(b) shows the profile of the function. The function was designed with two slopes [1 to 0.1 and 0.1 to 0, Fig. 15(b)] to monitor the performance for extremely heavy shadow conditions (between 0.1 and 0). After applying the shadow function to the simulated images and adding random noise [signal-to-noise ratio (SNR) 100], a simulated image set with shadows was obtained (Fig. 16). In Fig. 16, the right panel shows the light-shadow effect (1 to 0.1) for normal shadow conditions, and the left panel shows the heavy-shadow effect (0.1 to 0) for extreme conditions.

### 3.2.2 *Shadow removal*

Figure 17 shows a comparison of the standard, DPS, and calibrated RVI to the simulated image sets in which the white area represents vegetation distribution. For the standard RVI [Fig. 17(b)],
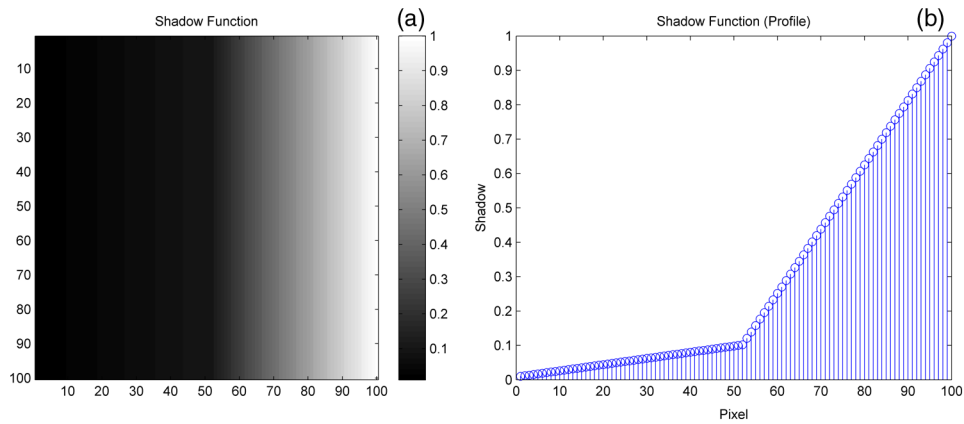
**Fig. 15** Simulated shading function. (a) Two-dimensional shadow function. (b) The profile of shadow function.
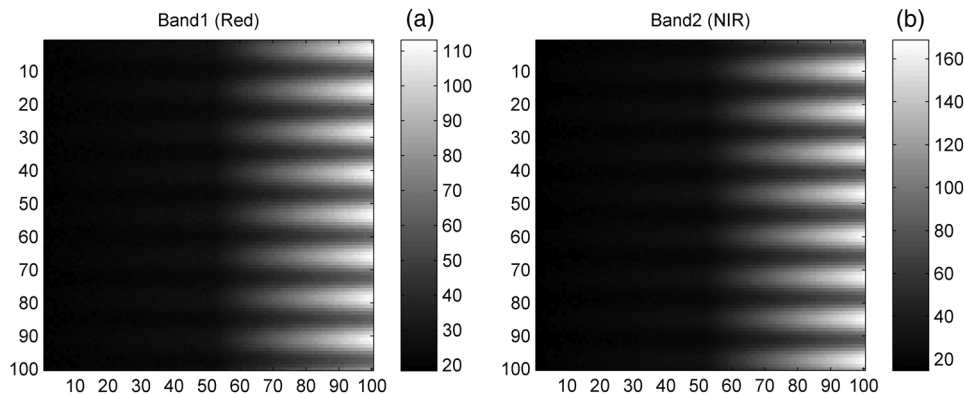


**Fig. 16** Two bands for the simulated image sets: (a) band 1 (red) and (b) band 2 (NIR).

areas with serious shadow effects (shadow function between 0 and 0.1) have very low values for both vegetated and nonvegetated areas. In Fig. 17(c), the result for DPS RVI has better adjustment; however, the heavily shaded vegetation is still not clearly identified. For calibrated RVI [Fig. 17(d)], the vegetated area is calibrated to the normal value even with serious shadow effects (shadow function between 0 and 0.1) and the nonvegetated region can be more easily recognized.

To evaluate the performance with the standard, DPS, and calibrated RVI, 10 vertical profiles were selected (Figs. 17 and 18) to represent 10 shadow levels. Figure 18 shows the shading function of the 10 levels, which include two groups: normal shadow (1 to 0.2514) and heavy shadow (0.0982 to 0.0262). The normal-shadow levels represent 10 to 100% and the heavy-shadow levels represent <10% of the spectral energy. The standard, DPS, and calibrated RVI are shown in Fig. 19. Before calibration, the standard RVI is very sensitive to the shadow effect, which caused the RVI to seriously underestimate the vegetated abundance at heavy-shadow conditions. DPS RVI shows more stable performance when processing vegetation detection. After calibration using the method described here (calibrated RVI), the detection performance has apparently improved even in some extremely heavy-shadow conditions.

## 4 Discussion

Many tropical and subtropical mountainous areas have high vegetation cover. In red-NIR spectra of remotely sensed images, the pure vegetated and nonvegetated pixels are the endmembers, and most of the image pixels will be distributed within these two endmembers. In addition to pixel mixture, in rugged terrain, most of the pixels also show topographic shadow effects. Therefore, a
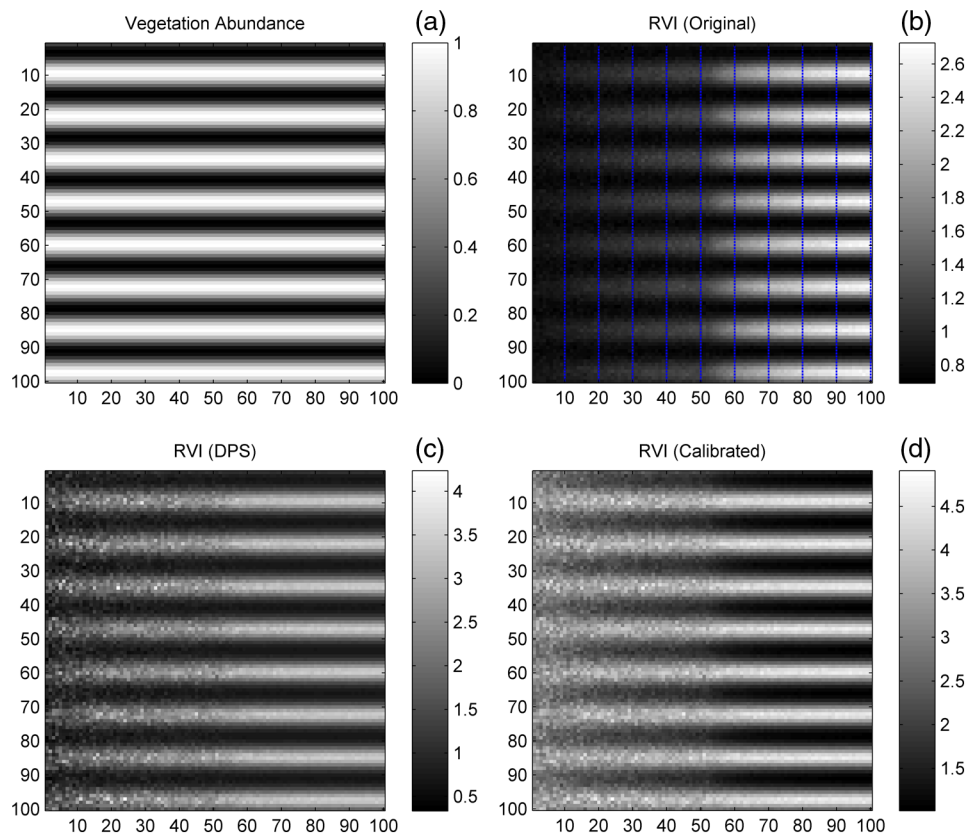
**Fig. 17** Comparisons of different adjustment approaches in simulated images. (a) Original vegetation abundance. (b) Standard RVI (the blue dotted lines represent the position of profile). (c) DPS RVI. (d) Calibrated RVI.

bispectral scatter plot (red-NIR) usually appears as an ideal triangle [Figs. 1, 2, 4, 7(b), 8, and 14(b)]. The triangular distribution (red-NIR scatter plot) is suited for using band ratios to reduce topographic shadow effects. The proposed method in this study was evaluated for the vegetation coverage in a mountainous area.

The real remote image test (SPOT5 satellite image) is shown in Fig. 11. Obviously, the standard RVI [Fig. 11(b)] has serious shadow effects. By using the color map [Fig. 11(a)] as ground truth to assess the standard RVI [Fig. 11(b)] and DPS RVI [Fig. 11(c)], a large number of errors are seen. The poor results gained from standard RVI and DPS RVI demonstrate that the ratio approach (RVI) is an efficient method for detection of mountain vegetation while simultaneously removing shadows. However, an inadequate processing ratio could cause fatal errors in classification through inadequate shadow removal. Using the calibrated RVI [Fig. 11(d)], the results show significant improvement, and the shadow effects are reduced. Using the color map [Fig. 11(a)] as a reference to compare the standard RVI [Fig. 11(b)], DPS RVI [Fig. 11(c)], and calibrated RVI [Fig. 11(d)], the calibrated RVI has a better ability to identify vegetated areas in areas of heavy shadow.

The real satellite image sets from two multispectral satellite sensors (SPOT5 and Formosat2, Fig. 12) in four mountainous areas of Taiwan (Jianshi, Guguan, Jiufen, and Caoling) were adopted for the experiments (Fig. 12). After RVIs (standard, DPS, and calibrated) processing with red and NIR bands, the ML was able to distinguish the vegetated and nonvegetated areas. The high resolution of color fusion maps (Formosat2: 2 m/pixel, SPOT5: 2.5 m/pixel) was employed for ground truth data to evaluate the performance of the RVIs. Table 1 shows that the calibrated RVI has higher accuracy than standard and DPS RVI in all four test sites for two satellite sensors. By analyzing the error pixels, we found that most of the errors in the shadow region of vegetated cover are underestimated. The calibrated RVI, therefore, has better ability to adjust shadow RVI to a normal level.
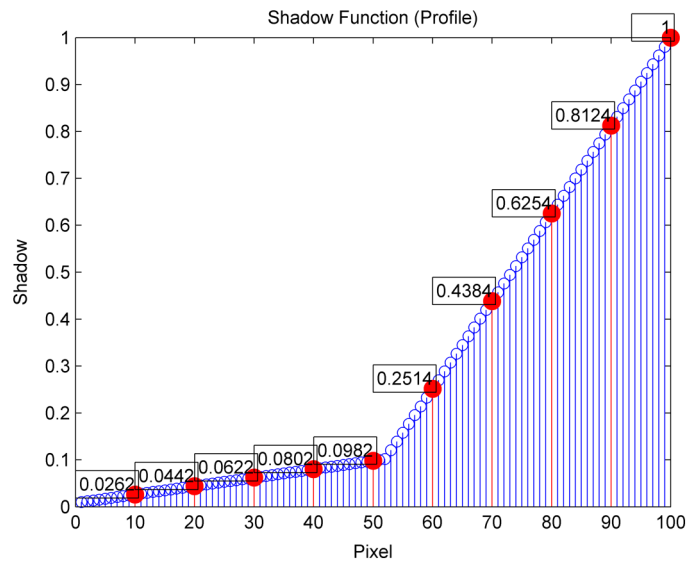
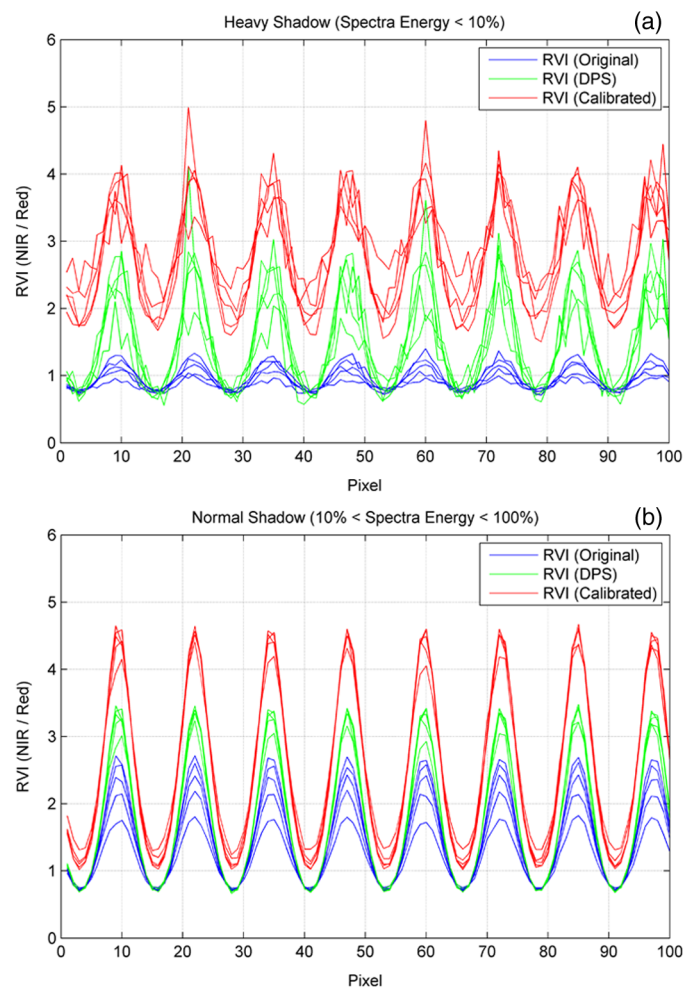**Fig. 18** The profiles of shading function.



**Fig. 19** Performance at heavy and normal shadow levels. Blue lines show the standard RVI, green lines show DPS RVI, and the red lines show the calibrated RVI. (a) Comparison of heavy shadow levels. (b) Comparison of normal shadow levels.

Results for the simulated image sets are shown in Figs. 17–19. Figure 17 shows that under light- (normal-) shadow conditions (1 to 0.1), the standard RVI, DPS RVI, and calibrated RVI have similar capabilities to recognize vegetated areas. When shadow effects reach heavy conditions (0.1 to 0), DPS RVI and calibrated RVI perform better when identifying vegetated cover. Figures 17 and 18 show the profiles of the results. Figure 19 demonstrates that standard RVI is oversensitive to terrain shadow effects, which might cause serious errors. However, DPS RVI and calibrated RVI demonstrate more stable characteristics for detecting vegetated cover. The comparison of DPS RVI and calibrated RVI also shows that the latter has better ability to distinguish vegetated from nonvegetated areas in normal shadow [Fig. 19(b)]. Further, in regions of heavy shadow, because of the low SNR, the performance of the calibrated RVI is slightly better than DPS RVI [Fig. 19(a)]. Because heavy shadow represents <10% of the spectral energy, such an extreme situation is not commonly seen.

This algorithm is based on the properties of a scatter plot of red-NIR bands from mountainous regions where topographic shadows occur. Owing to shadow effects, most classifications are distributed along an axis with a unique slope (ratio), and all pixels are ideally distributed within two endmembers (vegetated and nonvegetated). Therefore, the proposed algorithm is designed for images of typical mountainous areas. However, in reality, there are also some interference effects, such as clouds, surface-water features, and fog, in images of mountainous terrain. These interferences can affect the scatter plot with deviations from an ideal triangle, and the algorithm may be unable to select correct training samples for appropriate calibration. Furthermore, although the proposed algorithm used 0.2 and 0.6 as the target ratio value (NDVI), we recommend that the target ratio setting should be based on ground truth information to obtain accurate biomass content when using the calibrated RVI.

## 5 Conclusion

In this study, a simple and effective algorithm was developed to simultaneously reduce the effects of topographic shadows and distinguish between vegetated and nonvegetated cover. The proposed algorithm does not need any topographic information, but utilizes a simple calibration and the well-known band-ratio approach to obtain satisfactory performance. The red and NIR channels of SPOT5 and Formosat2 satellite image sets have been tested in experiments to show that the proposed method is significantly better than standard and DPS RVI. However, if this approach is used for remote images, including clouds or surface-water pixels, the effectiveness of the algorithm may be reduced.

## Acknowledgments

## References

1. R. A. Schowengerdt, *Remote Sensing: Models and Methods for Image Processing*, 2nd ed., pp. 36–185, Academic Press Limited, London (1997).
2. B. N. Holben and C. O. Justice, "The topographic effect on spectral response from nadir-pointing sensors," *Photogramm. Eng. Remote Sens.* **46**(9), 1191–1200 (1980).
3. R. W. Sjoberg and B. K. P. Horn, "Atmospheric effects in satellite imaging of mountainous terrain," *Appl. Opt.* **22**(11), 1702–1716 (1983).
4. C. Proy, D. Tanre, and P. Y. Deschamps, "Evaluation of topographic effects in remotely sensed data," *Remote Sens. Environ.* **30**(1), 21–32 (1989).
5. B. Leblon, L. Gallant, and H. Granberg, "Effects of shadowing types on ground-measured visible and near-infrared shadow reflectances," *Remote Sens. Environ.* **58**(3), 322–328 (1996).
6. D. W. Burgess, P. Lewis, and J.-P. A. L. Muller, "Topographic effects in AVHRR NDVI data," *Remote Sens. Environ.* **54**(3), 223–232 (1995).

7. B. K. P. Horn, "Hill shading and the reflectance map," *Proc. IEEE* **69**(1), 14–47 (1981).

8. R. O. Dubayah and J. Dozier, "Orthographic terrain views using data derived from digital elevation models," *Photogramm. Eng. Remote Sens.* **52**(4), 509–518 (1986).

9. P. T. Giles, M. A. Chapman, and S. E. Franklin, "Incorporation of a digital elevation model derived from stereoscopic satellite imagery in automated terrain analysis," *Comput. Geosci.* **20**(4), 441–460 (1994)..

10. C. O. Justice, S. W. Wharton, and B. N. Holben, "Application of digital terrain data to quantify and reduce the topographic effect on Landsat data," *Int. J. Remote Sens.* **2**(3), 213–230 (1981).

11. Y. Kawata, S. Ueno, and T. Kusaka, "Radiometric correction for atmospheric and topographic effects on Landsat MSS images," *Int. J. Remote Sens.* **9**(4), 729–748 (1988).

12. D. L. Civco, "Topographic normalization of Landsat Thematic Mapper digital imagery," *Photogramm. Eng. Remote Sens.* **55**(9), 1285–1294 (1989).

13. C. Conese, "Topographic normalization of TM scenes through the use of an atmospheric correction method and digital terrain models," *Photogramm. Eng. Remote Sens.* **59**(12), 1745–1753 (1993).

14. K. I. Itten and P. Meyer, "Geometric and radiometric correction of TM data of mountainous forested areas," *IEEE Trans. Geosci. Remote Sens.* **31**(4), 764–770 (1993).

15. P. M. Teillet, B. Guindon, and D. G. Goodenough, "On the slope-aspect correction of multispectral scanner data," *Can. J. Remote Sens.* **8**(2), 84–105 (1982).

16. Y. Li, P. Gong, and T. Sasagawa, "Integrated shadow removal based on photogrammetry and image analysis," *Int. J. Remote Sens.* **26**(18), 3911–3929 (2005).

17. J. D. Colby, "Topographic normalization in rugged terrain," *Photogramm. Eng. Remote Sens.* **57**(5), 531–537 (1991).

18. L. Xavier, V. Achard, and L. Poutier, "SIERRA: a new approach to atmospheric and topographic corrections for hyperspectral imagery," *Remote Sens. Environ.* **113**(8), 1664–1677 (2009).

19. D. Gu and A. Gillespie, "Topographic normalization of Landsat TM images of forest based on subpixel Sun-canopy-sensor geometry," *Remote Sens. Environ.* **64**(2), 166–175 (1998).

20. A. S. Scott, R. P. Derek, and A. C. Craig, "SCS+C: a modified Sun-canopy-sensor topographic correction in forested terrain," *IEEE Trans. Geosci. Remote Sens.* **43**(9), 2148–2159 (2005).

21. V. R. Kane et al., "Interpretation and topographic compensation of conifer canopy delf-shadowing," *Remote Sens. Environ.* **112**(10), 3820–3832 (2008).

22. S. D. Young, S. Kakarlapudi, and M. U. De Haag, "A shadow detection and extraction algorithm using digital elevation models and x-band weather radar measurements," *Int. J. Remote Sens.* **26**(8), 1531–1549 (2005).

23. B. Wang et al., "Automated detection and removal of clouds and their shadows from Landsat TM images," *IEICE Trans. Inf. Syst.* **E82-D**(2), 453–460 (1999).

24. H. Choi and R. Bindschadler, "Cloud detection in Landsat imagery of ice sheets using shadow matching technique and automatic normalized difference snow index threshold value decision," *Remote Sens. Environ.* **91**(2), 237–242 (2004).

25. N. Levin, E. Ben-Dor, and A. Karnieli, "Topographic information of sand dunes as extracted from shading effects using Landsat images," *Remote Sens. Environ.* **90**(2), 190–209 (2004).

26. R. Richter and A. Muller, "De-shadowing of satellite/airborne imagery," *Int. J. Remote Sens.* **26**(15), 3137–3148 (2005).

27. V. J. D. Tsai, "A comparative study on shadow compensation of color aerial images in invariant color models," *IEEE Trans. Geosci. Remote Sens.* **44**(6), 1661–1671 (2006).

28. D. Lu, "Detection and substitution of clouds/hazes and their cast shadows on IKONOS images," *Int. J. Remote Sens.* **28**(18), 4027–4035 (2007).

29. Y. Chen et al., "Shadow information recovery in urban areas from very high resolution satellite imagery," *Int. J. Remote Sens.* **28**(15), 3249–3254 (2007).

30. V. Arevalo, J. Gonzalez, and G. Ambrosio, "Shadow detection in colour high-resolution satellite images," *Int. J. Remote Sens.* **29**(7), 1945–1963 (2008).

31. W. Zhou et al., "Object-based land cover classification of shaded areas in high spatial resolution imagery of urban areas: a comparison study," *Remote Sens. Environ.* **113**(8), 1769–1777 (2009).

32. Y. Luo, A. P. Trishchenko, and K. V. Khlopenkov, "Developing clear-sky, cloud and cloud shadow mask for producing clear-sky composited at 250-meter spatial resolution for the seven MODIS land bands over Canada and North America," *Remote Sens. Environ.* **112**(12), 4167–4185 (2008).

33. G. D. Finlayson et al., "On the removal of shadows from images," *IEEE Trans. Pattern Anal. Mach. Intell.* **28**(1), 59–68 (2006).

34. A. Sanin, C. Sanderson, and B. C. Lovell, "Shadow detection: a survey and comparative evaluation of recent method," *Pattern Recognit.* **45**(4), 1684–1695 (2012).

35. P. T. Eliason, "Extraction of topographic and spectral albedo information from multispectral images," *Photogramm. Eng. Remote Sens.* **48**(11), 1571–1579 (1981).

36. R. E. Crippen, "The regression intersection method of adjusting image data for band ratioing," *Int. J. Remote Sens.* **8**(2), 137–155 (1987).

37. A. Shahtahmassebi et al., "Review of shadow detection and de-shadowing method in remote sensing," *Chin. Geogr. Sci.* **23**(4), 403–420 (2013).

38. B. Holben and C. Justice, "An examination of spectral band ratioing to reduce the topographic effect on remotely sensed data," *Int. J. Remote Sens.* **2**(2), 115–133 (1981).

39. R. E. Crippen, "The dangers of underestimating the importance of data adjustments in band ratioing," *Int. J. Remote Sens.* **9**(4), 767–776 (1988).

40. R. E. Crippen, R. G. Blom, and J. R. Heyada, "Directed band ratioing for the retention of perceptually-independent topographic expression in chromaticity-enhanced imagery," *Int. J. Remote Sens.* **9**(4), 749–765 (1988).

41. W. P. Gregory and D. J. Compagna, "Hyperspherical direction cosine transformation for separation of spectral and illumination information in digital scanner data," *Photogramm. Eng. Remote Sens.* **56**(4), 475–479 (1990).

42. M. L. Nirala and G. Venkatachalam, "Hyperspherical direction cosine transformation of remotely sensed data for separation of topographic expression of land use classification," *Int. J. Remote Sens.* **21**(11), 2203–2211 (2000).

43. Y. Deng et al., "Multi-scale linkages between topographic attributes and vegetation indices in a mountainous landscape," *Remote Sens. Environ.* **111**, 122–134 (2007).

44. L. R. Gaddis et al., "Decomposition of AVIRIS spectra: extraction of surface-reflectance, atmospheric, and instrumental components," *IEEE Trans. Geosci. Remote Sens.* **34**(1), 163–178 (1996).

45. J. Weier and D. Herring, "Measuring vegetation (NDVI & EVI)," 30 August 2000, http://earthobservatory.nasa.gov/Features/MeasuringVegetation/ (21 April 2014).

**Hung-Ming Kao** is a postdoctoral fellow at the Center for Space and Remote Sensing Research, National Central University, Taiwan. He received his BS degree in geology from the Chinese Culture University in 1997, his MS degree in geophysics from National Taiwan Ocean University in 1999, and his PhD degree in geosciences from the Institute of Applied Geosciences, National Taiwan Ocean University in 2009. His current research interests include remote sensing, signal processing, and geosciences.

Biographies of the other authors are not available.